ARTICLE

Textural properties prediction of KOH-activated carbon prepared from coal based on pyrolysis kinetics

Kai Wang[1] · Guoxin Lin[1] · Jun Meng[1] · Jiangmin Guo[1] · Bo Tan[1] · Shaojun Liu[1] · Qingyang Lin[1] · Xuecheng Wu[1] · Xiang Gao[1]

Abstract

Pyrolysis kinetics were used in this study to analyze the pore formation mechanism of coal activated with KOH. Experimental derivative thermogravimetry (DTG) curves were fitted using Achar and Coats–Redfern methods to obtain kinetic parameters, such as activation energies. The effects of heating rate and KOH ratio on the activation energy show similar trends. Another attempt was trying to correlate the activation energies with the textural properties. The direct fitting was initially used and the obtained activation energies showed little correlation with textural properties. Two improved methods, namely, single peak fitting and multi peak fitting, were introduced. The former only considered the interaction between KOH and coal, regardless of coal pyrolysis. The activation energies obtained showed linear relation with the total pore volumes/BET (Brunauer–Emmett–Teller) surface areas (R^2=0.94/0.99). The latter used Gaussian function to deconvolute the DTG curves, and then, each theoretical DTG peak could be correctly fitted. The positive linear correlation between the summed activation energies derived from surface reactions and metallic K intercalation and micropore volumes/surface areas was obtained (R^2=0.993/0.996). Therefore, the proposed methods could be successfully applied to design and analyze the textural properties of specific coals with KOH activation.

Keywords Coal activation · KOH · Textural properties · Activation energy

Introduction

Activated carbons (ACs) or analogous biochars are porous materials with well-developed textural properties and high chemical resistance, which are extensively used in several industrial processes, such as adsorption [1–3], catalysis [4, 5], sensing [6] and energy storage [7–9]. Therefore, the controllable preparation of high-performance AC with specific textural properties has attracted considerable interest from the industrial and academic fields. Carbohydrate [10, 11], biomass waste [12, 13], pitch [14, 15], polymers [16], and coal [17–22] are commonly chosen as carbon-containing precursors, and KOH is used as the activating agent. This process usually contains the mixing of precursors and KOH, pyrolysis under an inert atmosphere, and washing the residue with KOH (if necessary). Since precursors such as coal have unique properties, reactions between precursors and KOH during pyrolysis are extremely complicated. Therefore, the research progress has been adversely affected. Understanding activation energies of reactions can help reveal the mechanism of the process. Moreover, an in-depth understanding of the relationship between activation energy and textural properties can be obtained.

In the field of thermal analysis, thermogravimetric (TG) analysis is often used, which measures the mass loss per unit time and/or temperature for solid materials, such as coal and biomass, during the combustion and pyrolysis [10, 23–29]. In addition, kinetic parameters can be obtained through the quantitative analysis of TG curves. For example, based on the Arrhenius equation, TG experimental data should present a straight line with the slope proportional to the activation energy and the intercept representing the frequency factor [24, 28, 30, 31]. Cumming and Augnin [32] first proposed that the information obtained from the TG profiles could be

✉ Shaojun Liu
phoenix205@zju.edu.cn

[1] State Key Lab of Clean Energy Utilization, State Environmental Protection Center for Coal-Fired Air Pollution Control, Zhejiang University, Hangzhou 310027, China

Ⓐ Springer

used for the preliminary assessment of combustion and help in understanding the competitive behavior of coal blends. Knowledge of coal pyrolysis kinetics, such as co-pyrolysis with catalysts or individual pyrolysis, is also crucial for understanding internal reactions [33, 34]. This knowledge is necessary for reaction design and operation temperature control [35]. Thus, understanding coal decomposition and the interaction with KOH is important for understanding the thermochemical transformation process, which is crucial for developing an efficient reaction route. However, recent studies on the co-pyrolysis of coal and KOH in an inert atmosphere still lack information [18, 36].

This work aims to explore the pyrolysis kinetics of coal and KOH blends with different ratios using a TGA device and to reveal the relationship between the kinetic parameters and textural properties of the prepared ACs. These insights can be beneficial for optimizing the pyrolysis process and the preparation conditions of specific ACs with designed textural properties.

Materials and methods

Materials

Reed spring coal, which accounts for a considerable proportion of the proven coking coal reserves in China, was selected for this study due to its low degree of metamorphism and high volatile matter. The coal was ground and sieved to obtain a size range of 180–250 μm, dried at 110 °C for 24 h, and sealed in a glass container at room temperature before use. The proximate and ultimate analysis of the coal samples are listed in Table 1.

KOH was supplied by Sigma-Aldrich (Burlington, MA, USA). KOH and coal were manually mixed in appropriate proportions. The pyrolyzed samples were ground and sieved to obtain a particle size of 180–250 μm, dried at 110 °C for 24 h, and sealed before use. The sample with KOH/coal ratio of x:1 was labeled as AC-x.

TG tests

TG and derivative thermogravimetry (DTG) were used in this study to investigate and analyze the reaction processes and pyrolysis kinetics. Non-isothermal TG was performed using a thermal analyzer DSCQ-1000 (TA Instruments, New Castle, DE, USA) under a 50 mL/min N_2 from room temperature to 1000 °C at a heating rates ranging from 5 °C/min to 20 °C/min. To minimize heat and mass transfer effects, for all the samples, 5 mg of sample was dispersed uniformly on a flat crucible with a diameter and depth of 8 mm and 3 mm, respectively. To validate the results, repeated tests were conducted on each sample.

Characterization

The textural properties were characterized by N_2 adsorption–desorption at −196 °C using the ASAP 2020 system of Micromeritics Instrument Corporation (Norcross, GA, USA). Before the test, the pyrolyzed samples were degassed at 90 °C for 2 h, and then at 150 °C for 24 h to remove the moisture and other gas impurities adsorbed. The surface area (S_{BET}) was calculated using the Brunauer–Emmett–Teller (BET) equation. The total pore volume (V_{tot}) was measured at $P/P_0=0.99$. Micropore surface area (S_{mic}) and volume (V_{mic}) were determined via the t-plot method. The pore size distribution was calculated using density functional theory.

Kinetic analysis

In the non-isothermal kinetics studies, the relationship between temperature (T) and heating rate (β) is as follows [37–40]:

$$T = T_0 + \beta t, \tag{1}$$

where T_0 is the starting temperature, °C, t denotes the time, min, and the unit of β is °C/min.

The specific reaction rate is defined as

$$\frac{d\alpha}{dt} = kf(\alpha), \tag{2}$$

where

$$\alpha = \frac{W_0 - W}{W_0 - W_f}, \tag{3}$$

Table 1 Proximate and ultimate analysis of coal* (unit: %, in weight)

Coal type	Proximate analysis[a]				Ultimate analysis[b]				
	M	A	V	FC	C	H	N	S	O
Reed Spring Coal	1.18	8.12	38.37	52.33	70.76	4.67	1.24	0.47	9.76

*All the results are presented on dry basis; [a]M—moisture, A—ash, V—volatile matter, FC—fixed carbon; [b]C—carbon, H—hydrogen, N—nitrogen, S—sulphur, O—oxygen

$$k = A\exp\left(\frac{-E}{R_g T}\right),$$ (4)

where α is the fraction of the decomposed part; W_0, W, and W_f represent the initial mass, the residue mass at time t, and the final mass of the reactant as the reaction is completed, respectively. E denotes the activation energy, R_g indicates the gas constant, T refers to the absolute temperature, and A stands for the pre-exponential factor. $f(\alpha)$ is the hypothetical model of the reaction mechanism function of α.

In this study, Achar differential method and Coats–Redfern integral method were used to obtain kinetic parameters for pyrolysis. Moreover, the Bagchi method was applied to infer the reaction mechanism function.

Achar differential method

On the basis of Eqs. (1)–(4), the following formula can be obtained:

$$\frac{(d\alpha/dt)}{f(\alpha)} = A\exp\left(\frac{-E}{R_g T}\right).$$ (5)

By taking logarithms on both sides, the Achar equation can be obtained as follows [41–43]:

$$\ln\left[\frac{(d\alpha/dt)}{f(\alpha)}\right] = \ln A - \frac{E}{R_g T},$$ (6)

where the specific reaction rate can be also shown as

$$\frac{d\alpha}{dt} = \frac{\frac{dW}{dt}}{W_0 - W_f}.$$ (7)

$\ln[\frac{(d\alpha/dT)\beta}{f(\alpha)}]$ were linearly related to $1/T$ and kinetic parameters can be obtained from the slope and intercept of the line.

Coats–Redfern integral method

By replacing the integral expression of Eq. (5) with the Coats–Redfern approximate expression, the following formula can be obtained [37–40]:

$$g(\alpha) = \frac{A}{\beta} \frac{R_g T^2}{E}\left(1 - \frac{2RT}{E}\right)\exp\left(\frac{-E}{R_g T}\right),$$ (8)

where

$$g(\alpha) = \int_0^a \frac{d\alpha}{f(\alpha)}.$$ (9)

Considering that $2RT/E<1$, Eq. (8) can be simplified as the logarithmic form:

$$\log\left[\frac{g(\alpha)}{T^2}\right] = \log\left(\frac{AR}{\beta E}\right) - \frac{E}{R_g T}.$$ (10)

The kinetic parameters can be obtained from the slope and intercept of the line $[g(\alpha)/T^2]$ and $[1/T]$.

Function selection

Table 2 lists mathematical expressions (functions) for different kinetics. Using these functions and the aforementioned methods, the reaction mechanisms can be estimated from the DTG curves [40, 41, 43–51]. The first-order chemical reaction hypothesis (F_1 model) is commonly used in kinetic studies with TGA. In addition to this mechanism, other mechanisms focusing on reaction order (F_2–F_4 models), geometry (R_1–R_3 models), diffusion (D_1–D_4 models), and solid phase reaction (A_1–A_3 models) are also used to describe gas–solid reactions. According to Bagchi, the E and A values calculated by differential and integral methods should be similar, and correlation coefficients were used to evaluate the fitting results, as well as the optimal function [45, 46].

Single peak fitting

To determine the kinetic parameters of the interaction between KOH and coal, DTG curves of the blend were firstly fitted using the sum of coal pyrolysis and KOH–coal reactions as follows [24, 52]:

$$dm/dt_{sum} = x_1(dm/dt)_{pyrolysis} + x_2(dm/dt)_{reaction},$$ (11)

where $(dm/dt)_{pyrolysis}$ and $(dm/dt)_{reaction}$ are the mass loss rates of coal pyrolysis and the reaction of coal and KOH, respectively, and x_1 and x_2 denote the proportions of coal and KOH in the blend, respectively. Equation (11) was used to exclude the coal pyrolysis, and theoretical DTG curves only containing reactions between coal and KOH were obtained. Then, kinetic parameters could be calculated based on theoretical DTG curves.

Multi-peak fitting

Multipeak Gaussian fitting is often used for spectral or numerical analysis [47, 48]. This type of fitting is simple and effective for decomposing a complex curve containing multiple bumps or convexities into a number of Gaussian fitting peaks. To further understand the reaction mechanism between coal and KOH, multipeak Gaussian fitting method was used to de-convolute DTG curves, and the kinetic analysis was conducted based on each fitting peak to calculate corresponding activation energy.

Table 2 Mathematical expressions of different kinetics

Kinetics		$f(\alpha) = (\frac{d\alpha}{dt})/k$	$g(\alpha) = \int \frac{d\alpha}{f(\alpha)} = kt$
Based on the reaction order			
F_1	First-order, $n=1$	$1 - \alpha$	$-ln(1 - \alpha)$
F_2	1.5-order, $n=1.5$	$(1 - \alpha)^{3/2}$	$2[(1 - \alpha)^{-1/2} - 1]$
F_3	Second-order, $n=2$	$(1 - \alpha)^2$	$[(1 - \alpha)^{-1} - 1]$
F_4	Third-order, $n=3$	$(1 - \alpha)^3$	$0.5[(1 - \alpha)^{-2} - 1]$
Based on the geometry of reaction boundary			
R_1	Contractile reaction, $n=1/2$	$2(1 - \alpha)^{3/2}$	$(1 - \alpha)^{-1/2}$
R_2	Spherical symmetry model for phase boundary reaction, $n=1/3$	$3(1 - \alpha)^{2/3}$	$1 - (1 - \alpha)^{1/3}$
R_3	Symmetry model of phase boundary reaction, $n=1/4$	$4(1 - \alpha)^{3/4}$	$1 - (1 - \alpha)^{1/4}$
Based on the diffusion			
D_1	4D diffusion equation	$\frac{3}{2}[(1 - \alpha)^{-1/3} - 1]^{-1}$	$(1 - \frac{2}{3}\alpha) - (1 - \alpha)^{2/3}$
D_2	2D diffusion Jander equation	$(1 - \alpha)^{1/2}[1 - (1 - \alpha)^{1/2}]^{-1}$	$[1 - (1 - \alpha)^{1/2}]^2$
D_3	3D diffusion Jander equation	$\frac{3}{2}(1 - \alpha)^{2/3}[1 - (1 - \alpha)^{1/3}]^{-1}$	$[1 - (1 - \alpha)^{1/3}]^2$
D_4	3D diffusion Z. $-$ L. $-$ T. equation	$\frac{3}{2}(1 - \alpha)^{2/3}[1 - (1 - \alpha)^{-1/3}]^{-1}$	$[1 - (1 - \alpha)^{-1/3}]^2$
D_5	2D diffusion Valensi equation	$[-ln(1 - \alpha)]^{-1}$	$\alpha + (1 - \alpha)ln(1 - \alpha)$
Based on the solid phase reaction			
A_1	Avrami–Erofeev equation, $n=2/3$	$\frac{3}{2}(1 - \alpha)[-ln(1 - \alpha)]^{1/3}$	$[-ln(1 - \alpha)]^{2/3}$
A_2	Avrami–Erofeev equation, $n=2$	$\frac{1}{2}(1 - \alpha)[-ln(1 - \alpha)]^{-1}$	$[-ln(1 - \alpha)]^2$
A_3	Avrami–Erofeev equation, $n=3$	$\frac{1}{3}(1 - \alpha)[-ln(1 - \alpha)]^{-2}$	$[-ln(1 - \alpha)]^3$

Results and discussion

TG and DTG curves under N$_2$ atmosphere

Reed spring coal is a typical highly volatile coal with a volatile component accounting for more than 38% (Table 1). High volatiles components can evaporate during the heating process, resulting in considerable original textural properties, which are beneficial for the diffusion and reaction of KOH. Figure 1 shows the experimental TG and DTG curves for coal with/without KOH under N_2 atmosphere at different heating rates. The mass loss ratios of the mixtures were significantly higher than that of coal alone, and the ratio increased with increasing KOH ratio. The initial mass loss occurred at around 120 °C due to moisture evaporation, which is not shown in the figures, and the initial mass was defined as the mass after evaporation. The DTG curves demonstrated that two significant mass losses occurred at around 380–500 °C and 700–950 °C in the blended samples (AC-1, AC-2, AC-3), and only one mass loss at around 380–500 °C in the coal sample (AC-0). Mass loss at low temperature was possibly due to the release of volatiles during decomposition. For blended samples, it has been reported that KOH can break the chemical bonds

such as the alkyl-aryl bonds, enhancing the removal of some carbon components in the form of volatiles (CH_4, CO_2 or CO) [12]. Mass loss at high temperature was presumably ascribed to the complex reactions between coal and KOH, including the reduction of KOH, the production of K_2CO_3 and CO_x, and the evolution of H_2 [17, 19].

Table 3 shows the kinetic parameters calculated by Achar and Coats–Redfern methods, including temperature intervals marked as Range, the average temperature as T_a, reaction mechanism function (see Table 2) as Type, activation energy as E, pre-exponential factor as ln A and correlation coefficient as R^2. Using 15 functions (Table 2), activation energy and fitting correlation coefficient R^2 could be obtained by two methods. The function, which shows the least difference in energies for the two methods and the highest R^2, was chosen as the optimal one, and the results are listed in Table 3.

With the addition of KOH (AC-1), activation energy of the first mass loss significantly decreased, while that of the second mass loss increased compared to that of AC-0. As the content of KOH (AC-2/AC-3) continuously increased, maximum activation energy of the second mass loss increased, and the temperature at which maximum value was reached increased accordingly. In addition, fluctuation of activation energy to the temperature
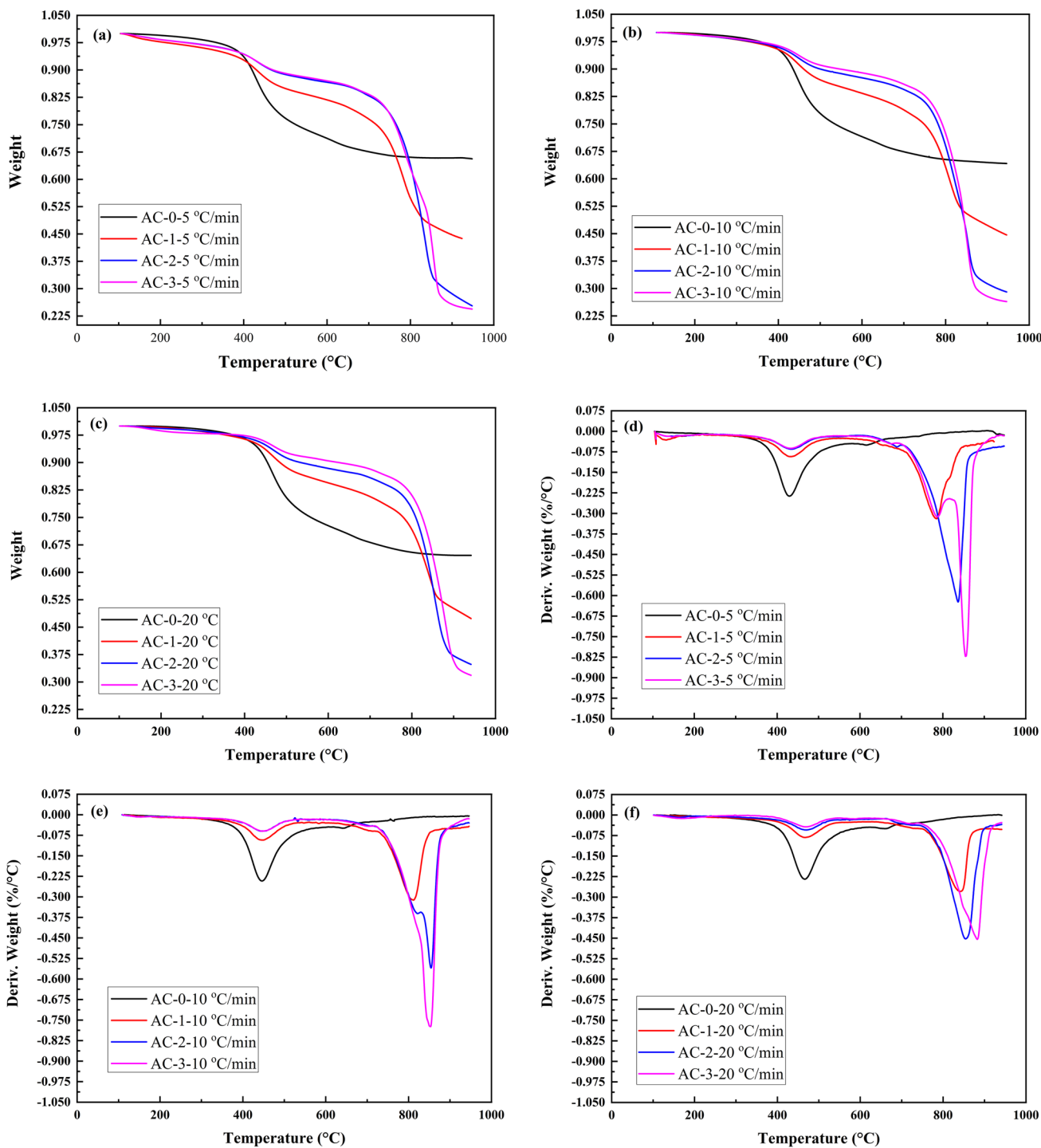
Fig. 1 TG and DTG curves of coal and KOH blends at different heating rates: TG curves at **a** 5 °C/min, **b** 10 °C/min, and **c** 20 °C/min; DTG curves at **d** 5 °C/min, **e** 10 °C/min, and **f** 20 °C/min (mass ratios of KOH to coal, including 0:1 [AC-0], 1:1 [AC-1], 2:1 [AC-2], and 3:1 [AC-3]). *TG* thermogravimetric, *DTG* derivative thermogravimetry

was mainly due to changed mechanism during pyrolysis, while fluctuation of that to the heating rate was ascribed to the temperature gradient from the inner to surface of the sample.

Textural properties of the samples

The literature has shown that different heating rates result in similar specific surface areas [11, 17, 18, 20, 36]. Hence,

Table 3 Kinetic parameters calculated by the Achar and Coats–Redfern methods with different heating rates

Sample	Range (°C)	T_a (°C)	Type	E (kJ/mol)	ln A	R^2
AC-0-5	105–377	241	A2	59.3	10.5	0.95
	377–490	434	A3	226.2	41.5	0.96
	490–601	546	A3	60.7	13.3	0.98
	601–632	617	D4	104.0	17.6	0.99
	632–940	786	F3	117.4	21.2	0.96
AC-1-5	105–380	243	A3	62.7	9.8	0.66
	380–499	440	A3	89.3	14.3	0.96
	499–628	564	A3	28.1	3.1	0.91
	628–657	643	A3	104.2	14.5	0.99
	657–722	690	A3	114.7	16.0	0.99
	722–826	774	A3	398.7	51.4	0.99
	826–940	883	A3	386.3	49.3	0.82
AC-2-5	105–366	236	A3	60.1	7.0	0.77
	366–432	399	A3	110.2	16.4	0.99
	432–636	534	A3	115.9	13.8	0.98
	698–764	731	D2	161.3	19.7	0.97
	764–871	818	A3	570.4	68.7	0.97
	871–940	906	A3	393.0	48.7	0.95
AC-3-5	105–376	241	A3	49.2	4.5	0.89
	376–482	429	A3	85.5	11.8	0.91
	482–713	598	A3	40.9	3.1	0.84
	713–805	759	A3	346.5	42.8	0.98
	805–831	818	A3	300.2	37.4	1.00
	831–874	853	A3	1170.0	133.0	0.97
	875–940	908	A3	924.4	106.0	0.86

Sample	Range (°C)	T_a (°C)	Type	E (kJ/mol)	ln A	R^2
AC-0-10	105–388	247	D4	70.6	10.1	0.96
	388–507	448	A3	236.6	42.1	0.96
	507–624	566	A3	59.5	12.6	0.98
	624–667	646	D4	83.0	14.0	0.94
	667–940	804	A3	101.9	18.5	0.91
AC-1-10	105–400	253	D4	57.9	7.0	0.92
	400–507	454	A3	120.0	19.0	0.90
	507–735	621	A3	55.1	7.3	0.93
	735–844	790	A3	417.0	52.6	0.97
	844–940	892	A3	337.4	43.0	0.91
AC-2-10	105–393	249	D4	46.3	3.6	0.89
	393–503	448	A3	105.1	14.7	0.90
	503–738	621	A3	48.5	4.3	0.89
	738–837	788	D2	268.0	32.0	0.99
	837–875	856	F3	622.0	73.8	0.93
	875–940	908	A3	424.0	52.3	0.93
AC-3-10	105–391	248	A3	75.6	8.8	0.88
	391–511	451	A3	97.7	13.0	0.87
	511–755	633	A3	59.4	5.5	0.89
	755–828	792	D1	279.5	32.2	0.99
	828–875	852	D4	920.1	104.2	0.98
	875–940	908	A3	427.1	53.1	0.95

Sample	Range (°C)	T_a (°C)	Type	E (kJ/mol)	ln A	R^2
AC-0-20	105–406	256	D4	84.4	12.6	0.96
	406–526	466	A3	248.5	43.1	0.96
	526–626	576	A3	60.2	12.6	0.99
	626–686	656	D4	96.8	15.8	0.97
	686–940	813	A3	165.7	26.8	0.93
AC-1-20	105–400	253	A3	103.2	15.4	0.91
	400–531	466	A3	138.4	21.5	0.93
	531–771	651	A3	59.8	7.9	0.93
	771–865	818	A3	491.5	59.8	0.98
	865–940	903	A3	488.3	58.7	0.85
AC-2-20	105–396	251	A3	73.0	7.9	0.86
	396–522	459	A3	126.2	17.9	0.95
	522–777	650	A3	56.1	5.4	0.86
	777–895	836	A3	666.1	77.8	0.98
	895–940	918	A3	729.0	83.6	0.87
AC-3-20	384–520	452	A3	129.2	17.6	0.95
	520–783	652	A3	61.9	5.5	0.88
	783–909	846	D3	386.9	43.6	0.98
	909–940	925	A3	964.8	107.0	0.87

Table 4 Textural properties of samples (heating rate: 5 °C/min)

Mass ratio of KOH: coal	BET specific surface areas (m²/g)	T-plot micropore specific surface areas (m²/g)	Total pore volume (mL/g)	T-plot micropore volume (mL/g)
0/1(AC-0)	104	98	0.0548	0.0467
1/1(AC-1)	792	713	0.4244	0.3802
2/1(AC-2)	978	757	0.5753	0.4049
3/1(AC-3)	709	543	0.4271	0.2908

BET Brunauer–Emmett–Teller

5 °C/min was selected. A series of ACs with different KOH ratios were prepared and characterized. In our previous work [53, 54], it was found that during the activation process, pore network generation was mainly caused by redox reactions between carbon and potassium compounds. Moreover, K atoms could also intercalate into carbon lattices, promoting microstructures in the carbon matrix. With increasing KOH content, these effects led to more drastic carbon pore evolution. Table 4 lists the BET analysis results for samples with different mass ratios of KOH to coal. Figure 2 presents the N_2 adsorption–desorption isotherms and pore size distributions. AC-0 showed an isotherm of low porosity materials. After mixing with KOH, all the samples exhibited Type I isotherms according to the IUPAC (International Union of Pure and Applied Chemistry) classification. With the increment of KOH content, nitrogen uptake at low relative pressure continuously increased up to AC-2. In addition, hysteresis curves could be observed at high relative pressures for samples AC-1 and AC-2, indicating the considerable mesopore formation. The drop of textural properties in sample AC-3 may be due to the excess transformation from micropore or mesopore to macropore, which is in line with results reported in the literature [55–59]. This speculation could be partially confirmed by the data listed in Table 4.

Relationship between the textural properties and kinetic parameters of single peak fitting

To further explore the interaction between KOH and coal, DTG curves in Fig. 1 were obtained. The curves show that the overall reaction could be generally divided into two stages. Using Eq. (11), coal pyrolysis was excluded mathematically, and new curves were obtained that mainly reflected reactions between coal and KOH, as shown in Fig. 3.

DTG results indicated that coal and KOH interacted with each other, and the effects varied with changes in the KOH ratios and heating rates. With the increasing content of KOH, DTG peaks shifted to the high temperature. The variation in heating rate changed the heat transfer, thereby affecting the interior reaction temperature.

Table 5 lists the kinetic parameters calculated by the Achar and Coats–Redfern methods. Figure 4 shows the relationships among activation energy, KOH ratio, and heating rate. The increasing heating rate increased the
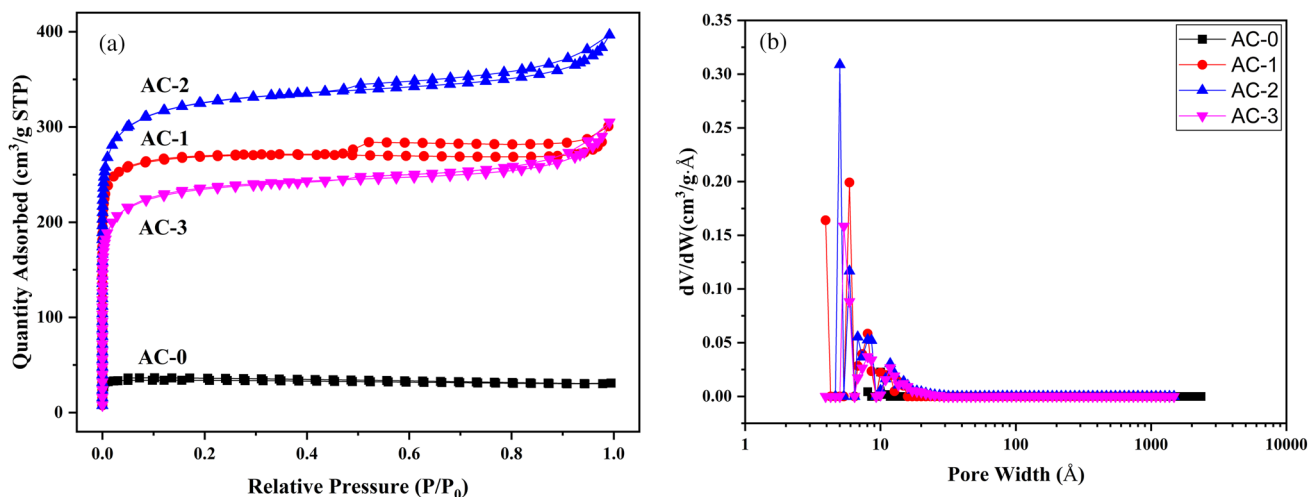

Fig. 2 Textural characterization of samples (heating rate: 5 °C/min). (**a**) Nitrogen adsorption isotherm. (**b**) Pore size distribution
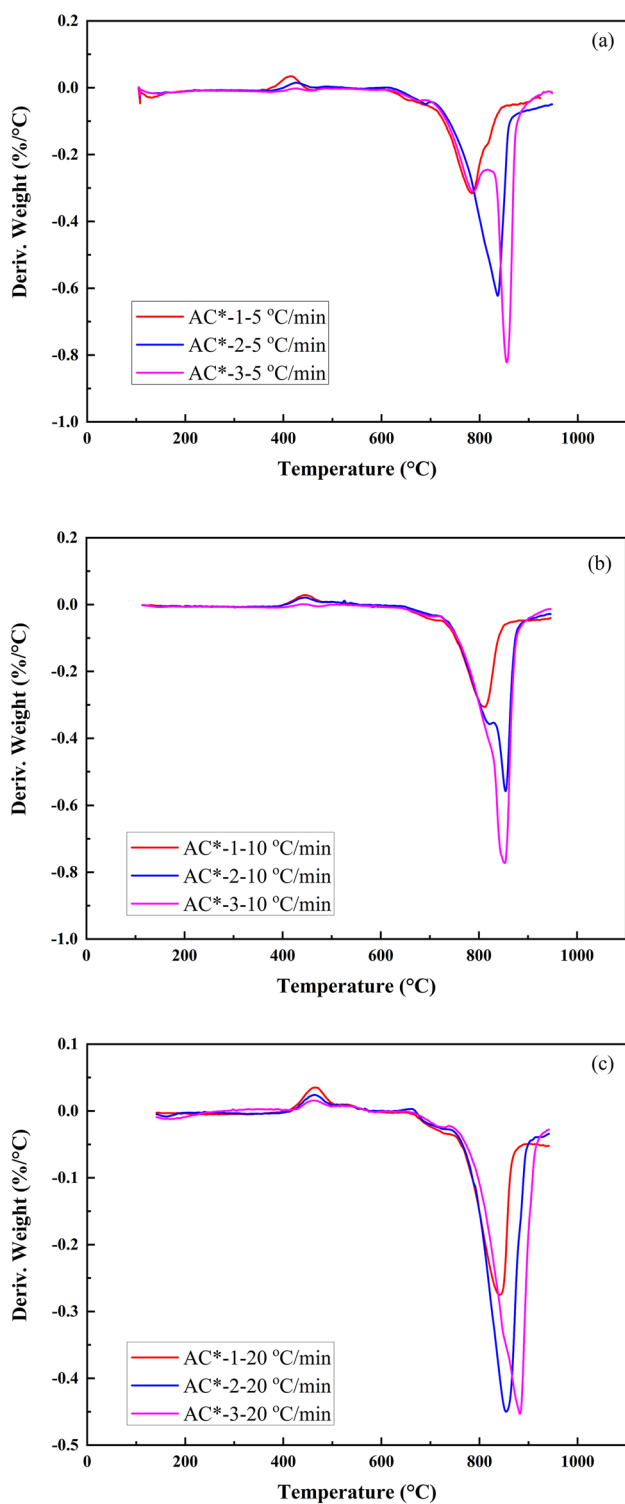
Fig. 3 Theoretical DTG curves only considering interaction between KOH and coal: **a** 5 °C/min, **b** 10 °C/min, **c** 20 °C/min (Mass ratios of KOH to coal, including 1:1 [AC*-1], 2:1 [AC*-2], and 3:1 [AC.*-3])

activation energy but reduced the fluctuation of activation energy. On one hand, as the heating rate increased from 5 °C/min to 20 °C/min, the resistance in heat transfer led to a

larger temperature difference between heating furnace and samples, thereby delaying the pyrolysis process and enhancing the pyrolysis temperature [60]. On the other hand, the decreased heating rate could provide additional time for the molten KOH to blend fully with coal [61, 62], thereby facilitating the reaction and decreasing the required activation energy. In addition, the variation of temperature range indicated the change of reaction mechanism, which reflected effect of heating rate on activation energy. Specifically, using 5 °C/min mechanism markedly differed from using the other two heating rates. With the increase of KOH ratio, the activation energy initially decreased and then increased, which indicated that an appropriate amount of KOH could promote the activation process, whereas the excessive addition of KOH would lead to side reactions and increase the activation energy.

Figure 5 presents the relationship of activation energy, specific surface area, and pore volume. A good linear correlation between the activation energies and the BET specific surface areas as well as total pore volumes could be observed (R^2=0.94/0.99). While as for micropores, a weak correlation is obvious. Thus, activation energies derived from single peak fitting could be used to explain the overall pore formation via reactions between KOH and coal. The increased activation energy required inhibited pore formation, which might be related to the macropores generated by the overreaction.

Relationship between the textural properties and kinetic parameters of multi peak fitting

In the previous section, the activation energy was correlated with the textural properties to a certain extent. To further analyze the relationship between textural properties and activation energy, the previous method was modified and the curves were deconvoluted by multipeak Gaussian fitting.

The deconvolution process was based on the related reactions. In our previous research [54], we found that the probable reactions between carbon and KOH include: (a) dehydration of KOH and the reaction with oxygen-containing functional groups on surface, as shown in Eqs. (12)–(13); (b) etching the carbon framework by redox reactions from KOH with carbon, as shown in Eqs. (14)–(15); and (c) the formation of K and K_2O, as shown in Eqs. (16)–(18).
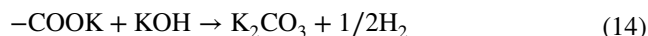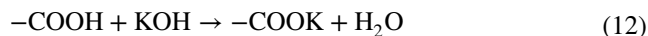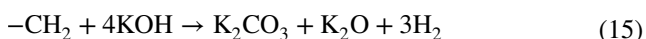
$$-COOH + KOH \rightarrow -COOK + H_2O \qquad (12)$$

$$2KOH \rightarrow K_2O + H_2O \qquad (13)$$

$$-COOK + KOH \rightarrow K_2CO_3 + 1/2H_2 \qquad (14)$$

Table 5 Kinetic parameters using single peak fitting

Sample	Range (°C)	$T_{Average}$ (°C)	Type	E (kJ/mol)	ln A	R^2
AC*1–5	684–880	782	D4	593.8	71.3	0.97
AC*2–5	712–946	829	F2	295.6	37.5	0.93
AC*3–5	709–895	802	D4	685.4	79.2	0.94
AC*1–10	727–876	802	A3	1058.6	123.9	0.97
AC*2–10	736–893	815	D4	850.2	97.2	0.96
AC*3–10	732–894	813	A3	1142.7	130.5	0.98
AC*1–20	762–890	826	A3	1262.4	143.6	0.97
AC*2–20	765–899	832	D4	1023.8	114.7	0.97
AC*3–20	772–916	844	A3	1272.7	141.1	0.97

$$-CH_2 + 4KOH \rightarrow K_2CO_3 + K_2O + 3H_2 \tag{15}$$

$$K_2CO_3 \rightarrow CO_2 + K_2O \tag{16}$$

$$K_2CO_3 + 2C \rightarrow 2K + 3CO \tag{17}$$

$$K_2O + C \rightarrow 2K + CO \tag{18}$$

Thus, the textural properties may largely depend on these reactions, especially for KOH-activated samples. At 350 °C–550 °C, volatile components began to evaporate (Peak 1[#]). At the same time, molten KOH (at a fusion temperature of 360 °C) would react with the macromolecular side chain of the coal to produce the initial porosity [61, 62]. At around 600–900 °C, the internal carbon activation reaction (Peak 2[#]) occurred. The molten KOH entering the pores reacted with the carbon matrix, and gas (CO, CO_2, H_2O and H_2) was produced [61–64]. Among them, CO_2 played a critical role in forming new microporous structures, whereas H_2O mainly ensured pore reaming and eventually promoted the formation of new mesopores and macropores [11, 17, 18, 20, 36]. At approximately 750 °C–950 °C, a large amount of metallic K was generated and overflowed (Peak 3[#]) [17, 63, 65, 66]. At this stage, the metallic K monomer moved through the layers of the carbon matrix, and the aromatic layer was stretched and deformed to form new micropores.

Therefore, on the basis of the reaction characteristics of these three stages, multipeak Gaussian fitting was performed, as shown in Fig. 6. The linear correlation obtained was above 0.98, and the peak temperature obtained roughly conformed to the abovementioned range. From the fitting results, the change in heating rate had minimal influence on the peak height, whereas the change in KOH ratio had a great influence on the peak height.

Table 6 lists the kinetic parameters calculated by the Achar and Coats–Redfern methods. Figure 7 shows the
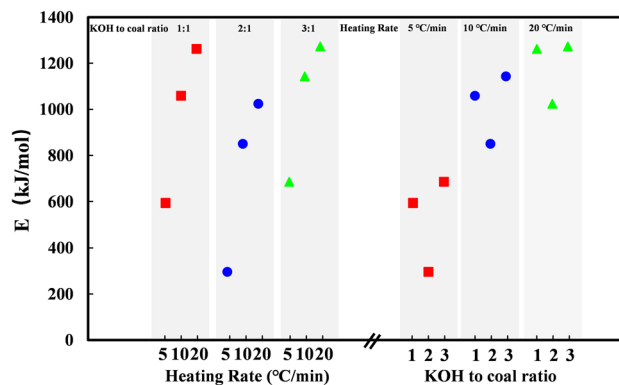

Fig. 4 The relationship among activation energy, KOH ratio, and heating rate using single peak fitting
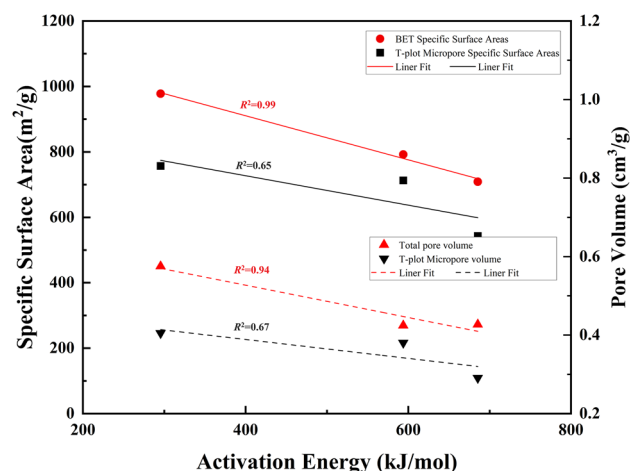

Fig. 5 Relationship among the activation energy of single peak fitting, pore volume, and specific surface area

relationship among activation energy, KOH ratio, and heating rate. With the increase of KOH ratio, the activation energy increased accordingly. Previous studies have
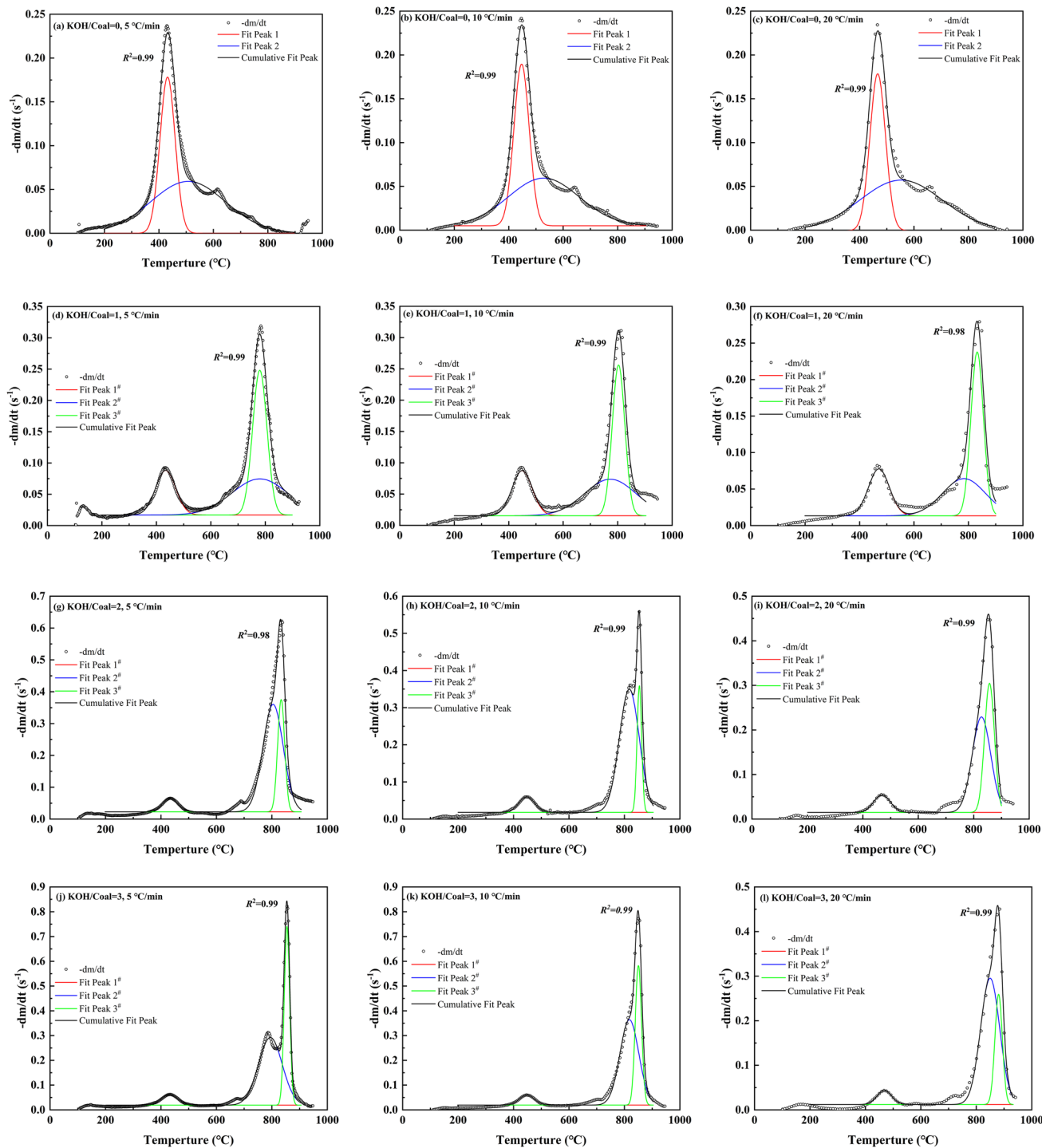
Fig. 6 Deconvolution of DTG curves using Gaussian function. **a** AC-0, 5 °C/min. **b** AC-0, 10 °C/min. **c** AC-0, 20 °C/min. **d** AC-1, 5 °C/min. **e** AC-1, 10 °C/min. **f** AC-1, 20 °C/min. **g** AC-2, 5 °C/min. **h** AC-2, 10 °C/min. **i** AC-2, 20 °C/min. **j** AC-3, 5 °C/min. **k** AC-3, 10 °C/min. **l** AC-3, 20 °C/min

shown that KOH melts at 360 °C [62, 66], forming a molten layer over coal particles. Then, the alkali species (molecules or ions) diffuse into the particles, and took part in the reactions. Experimental evidences observed in this work and in the literature validated this assumption. For example, the initial temperature for KOH/C reactions was 400 °C

Table 6 Kinetic parameters calculated after deconvolution of DTG curves

Sample	Range (°C)	Type	E	ln A (kJ/mol)	R^2	Sample	Range (°C)	Type	E	ln A (kJ/mol)	R^2
AC-0–5	373–490	D4	403.9	72.1	0.95	AC-0–10	384–510	D4	396.8	69.2	0.96
	304–710	D4	129.5	21.9	0.94		319–738	D4	130.2	21.3	0.94
AC-0–20	407–526	D4	434.9	73.9	0.96						
	335–771	D4	131.6	21.0	0.94						
AC-1–5	342–527	D4	254.1	45.9	0.96	AC-1–10	362–537	D4	283.9	50.0	0.96
	703–857	A2	634.1	77.4	0.94		738–868	D4	923.7	107.1	0.96
	532–924	A2	199.5	27.2	0.95		559–946	D4	227.2	28.2	0.95
AC-1–20	389–553	D4	319.7	54.5	0.96						
	771–893	A3	1307.0	147.8	0.94						
	625–942	D4	284.1	34.1	0.94						
AC-2–5	367–500	A2	288.0	53.6	0.95	AC-2–10	377–518	D4	338.8	59.6	0.95
	793–874	F2	861.8	100.3	0.96		827–880	F2	1324.4	148.5	0.96
	688–920	D4	541.8	63.2	0.97		752–933	D4	656.0	74.9	0.94
AC-2–20	409–529	D4	412.9	70.1	0.95						
	807–907	A3	1625.7	179.5	0.94						
	737–919	A2	607.1	70.7	0.96						
AC-3–5	366–498	A3	445.4	80.7	0.95	AC-3–10	387–509	A3	508.1	89.6	0.94
	823–886	A2	1831.4	201.9	0.93		814–887	D4	1828.9	201.2	0.97
	669–921	A3	672.1	79.9	0.96		783–922	D4	790.4	89.4	0.94
AC-3–20	425–512	D4	539.3	91.1	0.94						
	845–915	A3	2210.1	237.4	0.94						
	758–941	D4	786.8	87.5	0.97						

DTG derivative thermogravimetry

[17]. Thus, with the increase of KOH ratio, more energy was needed for melting, resulting in the rising of activation energies, as shown in Fig. 7. In comparison, the low heating rate could provide sufficient time for the full contact of molten KOH with the coal, thereby promoting the reaction. Therefore, the activation energy required was considerably low.

As the reactions in different stages had overlapping temperature ranges, the mass change in these stages was used as the weighting coefficient to calculate the activation energy when evaluating the relationship between activation energies and textural properties. Figure 8 shows the relationship among activation energy, specific surface area, and pore volume. The solid points are the combined activation energy values of Peaks 1# and 3#, and the hollow point was the value of Peak 3#. The micropore specific surface area and volume had a good linear correlation with the activation energy of Peak 3#, and the correlation coefficient was significantly improved using the activation energies of Peaks 1# and 3# (R^2=0.993/0.996). This result implied that the micropore formation was related
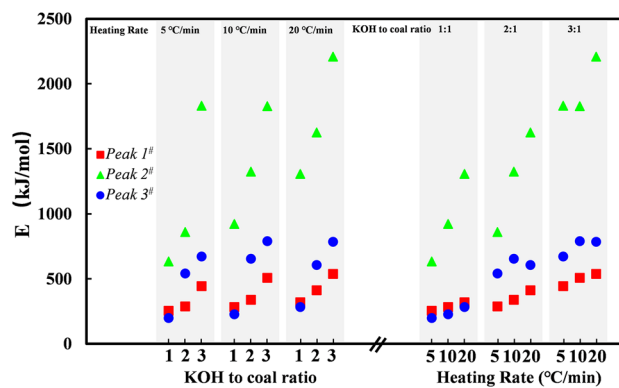

Fig. 7 Relationship among activation energy, KOH ratio, and heating rate using multi peak fitting

to the generation and overflow of metal *K*. At the same time, the initial pores also played a role in the formation of micropore structures, and the formation of micropores further developed on the initial pores.
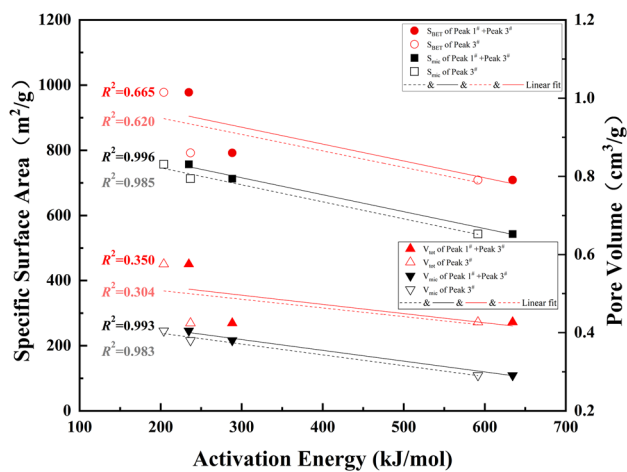
Fig. 8 Relationship among the activation energy using multi peak fitting, pore volume, and specific surface area

Conclusion

This work highlights the use of pyrolysis kinetics to determine the pore formation mechanism during coal activation with KOH. By adopting Achar differential and Coats–Redfern integral methods, experimental DTG curves were fitted based on mechanism functions, and kinetic parameters such as activation energies were obtained. The effects of heating rate and KOH ratio on the activation energy showed similar trends when one of the variables was fixed. Another attempt was to correlate the activation energies with the textural properties. The direct fitting was firstly employed, and the obtained activation energies showed little correlation with textural properties. Then, two different methods were used for deconvolution of DTG curves before fitting. The single peak fitting only considered the interaction between KOH and coal, regardless of coal pyrolysis. Linear correlation between the activation energies and total pore volumes/BET surface areas can be obtained (R^2=0.94/0.99), implying that the reactions between KOH and C strongly promoted the pore formation. The other multi peak fitting used Gaussian function to deconvolute the DTG curves, and then each theorical DTG peak was fitted using Achar and Coats–Redfern methods. It was found that the summed activation energies derived from surface reactions and metallic K intercalation were linearly related to the micropore volumes/surface areas (R^2=0.993/0.996). Moreover, the multi peak fitting revealed that the generation and overflow of metallic K played a vital role in the micropores formation. The proposed methods can be directly applied to the pore analysis and process design for coal activation with KOH.

Declarations

References

1. Masrura, S.U., Abbas, T., Heidari, H., et al. 2022. Density functional theory for selecting modifiers for enhanced adsorption of tetracycline in water by biochar. *Waste Disposal & Sustainable Energy* 5 (1): 25–35. https://doi.org/10.1007/s42768-022-00125-z.

2. Chauhan, S., Shafi, T., Dubey, B.K., et al. 2022. Biochar-mediated removal of pharmaceutical compounds from aqueous matrices via adsorption. *Waste Disposal & Sustainable Energy* 5 (1): 37–62. https://doi.org/10.1007/s42768-022-00118-y.

3. Abukari, A., Kaba, J.S., Dawoe, E., et al. 2022. A comprehensive review of the effects of biochar on soil physicochemical properties and crop productivity. *Waste Disposal & Sustainable Energy* 4 (4): 343–359. https://doi.org/10.1007/s42768-022-00114-2.

4. Al-Rahbi, A.S., and Williams, P.T. 2022. Decomposition of biomass gasification tar model compounds over waste tire pyrolysis char. *Waste Disposal & Sustainable Energy* 4 (2): 75–89. https://doi.org/10.1007/s42768-022-00103-5.

5. Ding, X., Huang, Y., Dong, X., et al. 2023. In-situ catalytic decomposition of emitted ammonia from municipal solid waste gasification by Ni–M bimetallic catalysts supported on sewage sludge-derived biochar. *Waste Disposal & Sustainable Energy* 5 (2): 113–124. https://doi.org/10.1007/s42768-022-00124-0.

6. Allende, S., Liu, Y., Zafar, M.A., et al. 2023. Nitrite sensor using activated biochar synthesised by microwave-assisted pyrolysis. *Waste Disposal & Sustainable Energy* 5 (1): 1–11. https://doi.org/10.1007/s42768-022-00120-4.

7. Bin, A.B.W., Yek, P.N.Y., Cheong, K.Y., et al. 2022. Utilization of microwave steam pyrolysis to produce biochar for thermal energy storage. *Waste Disposal & Sustainable Energy* 4 (4): 335–341. https://doi.org/10.1007/s42768-022-00116-0.

8. Zhang, J., Yang, H., Huang, Z., et al. 2023. Pore-structure regulation and heteroatom doping of activated carbon for supercapacitors with excellent rate performance and power density. *Waste Disposal & Sustainable Energy* 5 (3): 417–426. https://doi.org/10.1007/s42768-023-00155-1.

9. Zhou, J., Wei, K., Tian, L., et al. 2021. A universal synthesis of N, S, Cl-doped carbon materials directly from dye waste liquid for high performance lithium storage. *Waste Disposal & Sustainable Energy* 3 (2): 107–115. https://doi.org/10.1007/s42768-020-00059-4.

10. Zhang, L., Gu, H., Sun, H., et al. 2018. Molecular level one-step activation of agar to activated carbon for high performance supercapacitors. *Carbon* 132: 573–579. https://doi.org/10.1016/j.carbon.2018.02.100.

11. Bedin, K.C., Martins, A.C., Cazetta, A.L., et al. 2016. KOH-activated carbon prepared from sucrose spherical carbon:

Adsorption equilibrium, kinetic and thermodynamic studies for Methylene Blue removal. *Chemical Engineering Journal* 286: 476–484. https://doi.org/10.1016/j.cej.2015.10.099.

12. Liew, R.K., Azwar, E., Yek, P.N.Y., et al. 2018. Microwave pyrolysis with KOH/NaOH mixture activation: A new approach to produce micro-mesoporous activated carbon for textile dye adsorption. *Bioresource Technology* 266: 1–10. https://doi.org/10.1016/j.biortech.2018.06.051.

13. Sreńscek-Nazzal, J., Kamińska, W., Michalkiewicz, B., et al. 2013. Production, characterization and methane storage potential of KOH-activated carbon from sugarcane molasses. *Industrial Crops and Products* 47: 153–159. https://doi.org/10.1016/j.indcrop.2013.03.004.

14. Arami-Niya, A., Rufford, T.E., and Zhu, Z. 2016. Activated carbon monoliths with hierarchical pore structure from tar pitch and coal powder for the adsorption of CO_2, CH_4 and N_2. *Carbon* 103: 115–124. https://doi.org/10.1016/j.carbon.2016.02.098.

15. He, X., Li, R., Qiu, J., et al. 2012. Synthesis of mesoporous carbons for supercapacitors from coal tar pitch by coupling microwave-assisted KOH activation with a MgO template. *Carbon* 50 (13): 4911–4921. https://doi.org/10.1016/j.carbon.2012.06.020.

16. Wickramaratne, N.P., and Jaroniec, M. 2013. Importance of small micropores in CO_2 capture by phenolic resin-based activated carbon spheres. *Journal of Materials Chemistry A* 1 (1): 112–116. https://doi.org/10.1039/c2ta00388k.

17. Lillo-Ródenas, M.A., Cazorla-Amorós, D., and Linares-Solano, A. 2003. Understanding chemical reactions between carbons and NaOH and KOH. *Carbon* 41 (2): 267–275. https://doi.org/10.1016/s0008-6223(02)00279-8.

18. Zuo, L., Ai, J., Fu, H., et al. 2016. Enhanced removal of sulfonamide antibiotics by KOH-activated anthracite coal: Batch and fixed-bed studies. *Environmental Pollution* 211: 425–434. https://doi.org/10.1016/j.envpol.2015.12.064.

19. Kopac, T., Kırca, Y., and Toprak, A. 2017. Synthesis and characterization of KOH/boron modified activated carbons from coal and their hydrogen sorption characteristics. *International Journal of Hydrogen Energy* 42 (37): 23606–23616. https://doi.org/10.1016/j.ijhydene.2017.01.195.

20. Labus, K., Gryglewicz, S., and Machnikowski, J. 2014. Granular KOH-activated carbons from coal-based cokes and their CO_2 adsorption capacity. *Fuel* 118: 9–15. https://doi.org/10.1016/j.fuel.2013.10.042.

21. Xiao, X., Liu, D., Yan, Y., et al. 2015. Preparation of activated carbon from Xinjiang region coal by microwave activation and its application in naphthalene, phenanthrene, and pyrene adsorption. *Journal of the Taiwan Institute of Chemical Engineers* 53: 160–167. https://doi.org/10.1016/j.jtice.2015.02.031.

22. Wang, J., Jin, L., Li, Y., et al. 2016. Effect of air pre-oxidization on coal-based activated carbon for methane decomposition to hydrogen. *International Journal of Hydrogen Energy* 41 (25): 10661–10669. https://doi.org/10.1016/j.ijhydene.2016.04.021.

23. Wang, C., Wang, F., Yang, Q., et al. 2009. Thermogravimetric studies of the behavior of wheat straw with added coal during combustion. *Biomass and Bioenergy* 33 (1): 50–56. https://doi.org/10.1016/j.biombioe.2008.04.013.

24. Gil, M.V., Casal, D., Pevida, C., et al. 2010. Thermal behaviour and kinetics of coal/biomass blends during co-combustion. *Bioresource Technology* 101 (14): 5601–5608. https://doi.org/10.1016/j.biortech.2010.02.008.

25. Mureddu, M., Dessì, F., Orsini, A., et al. 2018. Air- and oxygen-blown characterization of coal and biomass by thermogravimetric analysis. *Fuel* 212: 626–637. https://doi.org/10.1016/j.fuel.2017.10.005.

26. Skodras, G., Grammelis, P., and Basinas, P. 2007. Pyrolysis and combustion behaviour of coal-MBM blends. *Bioresource Technology* 98 (1): 1–8. https://doi.org/10.1016/j.biortech.2005.12.007.

27. Idris, S.S., Abd Rahman, N., Ismail, K., et al. 2010. Investigation on thermochemical behaviour of low rank Malaysian coal, oil palm biomass and their blends during pyrolysis via thermogravimetric analysis (TGA). *Bioresource Technology* 101 (12): 4584–4592. https://doi.org/10.1016/j.biortech.2010.01.059.

28. Buratti, C., Barbanera, M., Bartocci, P., et al. 2015. Thermogravimetric analysis of the behavior of sub-bituminous coal and cellulosic ethanol residue during co-combustion. *Bioresource Technology* 186: 154–162. https://doi.org/10.1016/j.biortech.2015.03.041.

29. Junga, R., Knauer, W., Niemiec, P., et al. 2017. Experimental tests of co-combustion of laying hens manure with coal by using thermogravimetric analysis. *Renewable Energy* 111: 245–255. https://doi.org/10.1016/j.renene.2017.03.099.

30. Shen, D.K., Gu, S., Luo, K.H., et al. 2009. Kinetic study on thermal decomposition of woods in oxidative environment. *Fuel* 88 (6): 1024–1030. https://doi.org/10.1016/j.fuel.2008.10.034.

31. Zhou, L., Wang, Y., Huang, Q., et al. 2006. Thermogravimetric characteristics and kinetic of plastic and biomass blends co-pyrolysis. *Fuel Processing Technology* 87 (11): 963–969. https://doi.org/10.1016/j.fuproc.2006.07.002.

32. Cumming, J.W., and McLaughlin, J. 1982. The thermogravimetric behaviour of coal. *Thermochimica Acta* 57 (3): 253–272. https://doi.org/10.1016/0040-6031(82)80037-3.

33. Mayoral, M.C., Izquierdo, M.T., Andrés, J.M., et al. 2001. Different approaches to proximate analysis by thermogravimetry analysis. *Thermochimica Acta* 370 (1): 91–97. https://doi.org/10.1016/S0040-6031(00)00789-9.

34. David, J., Steinmetz, Z., Kucerik, J., et al. 2018. Quantitative analysis of poly(ethylene terephthalate) microplastics in soil via thermogravimetry-mass spectrometry. *Analytical Chemistry* 90 (15): 8793–8799. https://doi.org/10.1021/acs.analchem.8b00355.

35. Chen, W.-H., and Kuo, P.-C. 2010. A study on torrefaction of various biomass materials and its impact on lignocellulosic structure simulated by a thermogravimetry. *Energy* 35 (6): 2580–2586. https://doi.org/10.1016/j.energy.2010.02.054.

36. Meshram, P., Purohit, B.K., Sinha, M.K., et al. 2015. Demineralization of low grade coal—A review. *Renewable and Sustainable Energy Reviews* 41: 745–761. https://doi.org/10.1016/j.rser.2014.08.072.

37. Li, Z., Liu, C., Chen, Z., et al. 2009. Analysis of coals and biomass pyrolysis using the distributed activation energy model. *Bioresource Technology* 100 (2): 948–952. https://doi.org/10.1016/j.biortech.2008.07.032.

38. Ca, Wang, Liu, Y., Zhang, X., et al. 2011. A study on coal properties and combustion characteristics of blended coals in Northwestern China. *Energy & Fuel* 25 (8): 3634–3645. https://doi.org/10.1021/ef200686d.

39. Sadeghi, M., Nemati, A., Ghavimi, A., et al. 2016. Thermodynamic analysis and multi-objective optimization of various ORC (organic Rankine cycle) configurations using zeotropic mixtures. *Energy* 109: 791–802. https://doi.org/10.1016/j.energy.2016.05.022.

40. Naqvi, S.R., Tariq, R., Hameed, Z., et al. 2019. Pyrolysis of high ash sewage sludge: Kinetics and thermodynamic analysis using Coats-Redfern method. *Renewable Energy* 131: 854–860. https://doi.org/10.1016/j.renene.2018.07.094.

41. Yu, J., Zeng, X., Zhang, J., et al. 2013. Isothermal differential characteristics of gas–solid reaction in micro-fluidized bed reactor. *Fuel* 103: 29–36. https://doi.org/10.1016/j.fuel.2011.09.060.

42. Liu, S., Chen, M., Hu, Q., et al. 2013. The kinetics model and pyrolysis behavior of the aqueous fraction of bio-oil. *Bioresource Technology* 129: 381–386. https://doi.org/10.1016/j.biortech.2012.11.006.

43. Deng, J., Yang, Y., Zhang, Y.-N., et al. 2018. Inhibiting effects of three commercial inhibitors in spontaneous coal combustion. *Energy* 160: 1174–1185. https://doi.org/10.1016/j.energy.2018.07.040.

44. Niu, S., Yu, H., Zhao, S., et al. 2019. Apparent kinetic and thermodynamic calculation for thermal degradation of stearic acid and its esterification derivants through thermogravimetric analysis. *Renewable Energy* 133: 373–381. https://doi.org/10.1016/j.renene.2018.10.045.

45. Duan, W., Yu, Q., Xie, H., et al. 2017. Pyrolysis of coal by solid heat carrier-experimental study and kinetic modeling. *Energy* 135: 317–326. https://doi.org/10.1016/j.energy.2017.06.132.

46. Brighenti, M., Grigiante, M., Antolini, D., et al. 2017. An innovative kinetic model dedicated to mild degradation (torrefaction) of biomasses. *Applied Energy* 206: 475–486. https://doi.org/10.1016/j.apenergy.2017.08.122.

47. Bai, F., Guo, W., Lü, X., et al. 2015. Kinetic study on the pyrolysis behavior of Huadian oil shale via non-isothermal thermogravimetric data. *Fuel* 146: 111–118. https://doi.org/10.1016/j.fuel.2014.12.073.

48. Moine, E.C., Groune, K., El Hamidi, A., et al. 2016. Multistep process kinetics of the non-isothermal pyrolysis of Moroccan Rif oil shale. *Energy* 115: 931–941. https://doi.org/10.1016/j.energy.2016.09.033.

49. Azam, M., Jahromy, S.S., Raza, W., et al. 2019. Comparison of the combustion characteristics and kinetic study of coal, municipal solid waste, and refuse-derived fuel: Model-fitting methods. *Energy Science & Engineering* 7 (6): 2646–2657. https://doi.org/10.1002/ese3.450.

50. Siregar, S.R.H., Nursani, D., Setyawan, M.I.B., et al. 2021. Study of kinetic and thermal decomposition from municipal solid waste pellets using model-fitting methods. *IOP Conference Series: Materials Science and Engineering* 1173 (1): 012033. https://doi.org/10.1088/1757-899x/1173/1/012033.

51. Boumanchar, I., Chhiti, Y., M'Hamdi Alaoui, F.E., et al. 2019. Investigation of (co)-combustion kinetics of biomass, coal and municipal solid wastes. *Waste Management* 97: 10–18. https://doi.org/10.1016/j.wasman.2019.07.033.

52. Qin, H., Wang, W., Liu, H., et al. 2017. Thermal behavior research for co-combustion of furfural residue and oil shale semi-coke. *Applied Thermal Engineering* 120: 19–25. https://doi.org/10.1016/j.applthermaleng.2017.03.111.

53. Yu, X., Liu, S., Lin, G., et al. 2020. KOH-activated hydrochar with engineered porosity as sustainable adsorbent for volatile organic compounds. *Colloids and Surfaces A: Physicochemical and Engineering Aspects* 588: 124372. https://doi.org/10.1016/j.colsurfa.2019.124372.

54. Yu, X.N., Liu, S.J., Lin, G.X., et al. 2019. Promotion effect of KOH surface etching on sucrose-based hydrochar for acetone adsorption. *Applied Surface Science* 496: 11. https://doi.org/10.1016/j.apsusc.2019.143617.

55. Ligero, A., Calero, M., Pérez, A., et al. 2023. Low-cost activated carbon from the pyrolysis of post-consumer plastic waste and the application in CO_2 capture. *Process Safety and Environmental Protection* 173: 558–566. https://doi.org/10.1016/j.psep.2023.03.041.

56. Lin, L., Zheng, Z., Li, X., et al. 2023. Design strategy for porous carbon nanomaterials from rational utilization of natural rubber latex foam scraps. *Industrial Crops and Products* 192: 116036. https://doi.org/10.1016/j.indcrop.2022.116036.

57. Pourbaba, R., Abdulkhani, A., Rashidi, A., et al. 2024. Sustainable production of hierarchically porous carbon from lignin-acrylic acid copolymers. *Journal of Polymers and the Environment*. https://doi.org/10.1007/s10924-023-03177-2.

58. Gao, Y., Huo, Y., Chen, M., et al. 2023. Phenolic based porous carbon fibers with superior surface area and adsorption efficiency for radioactive protection. *Advanced Fiber Materials* 5 (4): 1431–1446. https://doi.org/10.1007/s42765-023-00284-6.

59. Goskula, S., Siliveri, S., Gujjula, S.R., et al. 2023. Development of activated sustainable porous carbon adsorbents from Karanja shell biomass and their CO_2 adsorption. *Biomass Conversion and Biorefinery*. https://doi.org/10.1007/s13399-023-05198-2.

60. Tang, Q., Zheng, Y.Y., Wang, T.F., et al. 2014. Study on the kinetics of plant oil asphalt pyrolysis using thermogravimetry and the distributed activation energy model. *Energy & Fuels* 28 (3): 2035–2040.

61. Gong, L., and Bao, A. 2023. High-value utilization of lignin to prepare NO-codoped porous carbon as a high-performance adsorbent for carbon dioxide capture. *Journal of CO2 Utilization* 68: 102374. https://doi.org/10.1016/j.jcou.2022.102374.

62. Ateş, A. 2021. The effect of microwave and ultrasound activation on the characteristics of biochar produced from tea waste in the presence of H_3PO_4 and KOH. *Biomass Conversion and Biorefinery* 13 (10): 9075–9094. https://doi.org/10.1007/s13399-021-01838-7.

63. Sun, Q., Liu, T., Wen, T., et al. 2023. Porous carbon tubes from recycling waste COVID-19 masks for optimization of 8 mol% Y_2O_3-doped tetragonal zirconia polycrystalline nanopowder. *Materials Today Chemistry* 30: 101526. https://doi.org/10.1016/j.mtchem.2023.101526.

64. Wu, Y., Guo, Y., Su, R., et al. 2022. Hierarchical porous carbon with an ultrahigh surface area for high-efficient iodine capture: Insights into adsorption mechanisms through experiments, simulations and modeling. *Separation and Purification Technology* 303: 122237. https://doi.org/10.1016/j.seppur.2022.122237.

65. Park, J.Y., Hur, J., Yi, S.-H., et al. 2024. Porous carbon from polyvinylidene chloride or polyvinylidene fluoride with ZnO, $Mg(OH)_2$, and KOH for supercapacitor. *Carbon Letters* 34 (2): 677–690. https://doi.org/10.1007/s42823-023-00670-5.

66. Montes, V., Xiao, Y., Wu, J., et al. 2022. Distribution of potassium during chemical activation of petroleum coke: Electron microscopy evidence and links to phase behaviour. *The Canadian Journal of Chemical Engineering* 101 (5): 2621–2632. https://doi.org/10.1002/cjce.24677.